



Phase diversity algorithm with high noise robust based on deep denoising convolutional neural network

DEQUAN LI,^{1,2,*} SHUYAN XU,¹ DONG WANG,¹ AND DEJIE YAN¹

¹Space Optics Department, Changchun Institute of Optics, Fine Mechanics and Physics, Chinese Academy of Sciences, Changchun, Jilin 130033, China

²University of Chinese Academy of Sciences, Beijing 100049, China

*lidequan@ciomp.ac.cn

Abstract: The wave-front phase expanded on the Zernike polynomials is estimated from a pair of images by the use of a maximum-likelihood approach, the in-focus image and the defocus image, which contaminated by noise, will greatly reduce the solution accuracy of the phase diversity (PD) algorithm. In the study, we introduce the deep denoising convolutional neural networks (DnCNNs) into the image preprocessing of PD to denoise the in-focus image and defocus the image containing gaussian white noise to improve the robustness of PD to noise. The simulation results show that the composite PD algorithm with DnCNNs is better than the traditional PD algorithm in both RMSE of phase estimation and SSIM, and the mean of the RMSE of the phase estimation of the improved PD algorithm is reduced by 78.48%, 82.35%, 71.09% and 73.67% compared with the mean of the RMSE of the phase estimation of the traditional PD algorithm. The well-trained DnCNNs runs fast, which does not increase the running time of traditional PD algorithms, and the compound approach may be widely used in various domains, such as the measurements of intrinsic aberrations in optical systems and compensations for atmospheric turbulence.

© 2019 Optical Society of America under the terms of the [OSA Open Access Publishing Agreement](#)

1. Introduction

Wavefront sensing is an important part of adaptive optics systems. There are some wavefront sensing methods which depend on the external hardware facilities [1,2]. The others are based on the measured images, only. The PD algorithm [3] is in this second category. It has the advantage of the simple optical path. With phases expanded in Zernike polynomials [4] and with a pair of images, the PD algorithm can estimate both the unknown phase and the object under observation. The PD algorithm was proposed by Gonsalves in 1982 [3] and was improved by Paxman, et al. in 1994 [5] and by Lee, et al. in 1997 [6]. The theory is enhanced papers by Akaike [7] and Sobieranski, et al [8]. The main goal of PD is to reconstruct the wavefront by solving an optimization problem. For the past many years, this method has reached a wide range of applications [9]. However, noise-contaminated images will greatly reduce the accuracy and success rate of the PD algorithm. In the real environment, Gaussian noise is a very common image noise, especially when most sources of noise are thermal noise. Therefore, in this paper, we mainly verify the processing ability of the improved PD algorithm for in-focus images and defocus images containing Gaussian white noise.

2. Principles

For a space-invariant incoherent imaging system, the relations of the focus image collected in the focus surface and the object in the spatial domain in this optical system are [7]:

$$i(x, y) = o(x, y) * PSF(x, y). \quad (1)$$

the relationship in the frequency domain is:

$$I(u, v) = O(u, v) \bullet OTF(u, v). \quad (2)$$

And $PSF(u, v)$ can be obtained by the inverse Fourier transform of generalized pupil function

$$PSF(x, y) = \left| FT^{-1}(P(u, v)) \right|^2. \quad (3)$$

In the above equations, the variables x, y are all variables in the spatial domain. $o(x, y)$ is the distribution functions of the two-dimensional object. $i(x, y)$ is the intensity distribution of the image on the ideal focal plane. $PSF(x, y)$ is optical system point spread function corresponding to the intensity distribution of an ideal focal plane image. $P(u, v)$ is generalized pupil function for an optical system. $FT^{-1}()$ is a two-dimensional inverse Fourier transform operation.

The pupil function of the optical system can be represented by the modulus value $A(u, v)$ and the phase $\phi(u, v)$. The equation is:

$$P(u, v) = A(u, v) \exp(i\phi(u, v)). \quad (4)$$

Assuming that the pupil of the optical system is an ideal pupil, the module value is in the range of $\sqrt{u^2 + v^2} \leq D$, $A(u, v) = 1$, the module value is in the range of $\sqrt{u^2 + v^2} > D$, $A(u, v) = 0$. In the equation, $\phi(u, v)$ is the unknown wavefront aberration. The phase diversity function can be developed by the Zernike polynomials with orthogonality in the unit circle [8].

$$\phi(u, v) = \sum_i^N a_i c_i(u, v). \quad (5)$$

Where N is the number of the selected Zernike polynomials. The coefficients $c_1 - c_3$ stand for piston, tip, and tilt of the wavefront aberration, which have no effect on the quality of the image and can be eliminated by spatial positional transformation, so in this article we don't consider $c_1 - c_3$. Of course, we can also consider $c_1 - c_3$, and the experiment shows that the comparison results are similar.

Similarly, the relations of the defocus image collected in the defocus surface and the object in the spatial domain in this optical system are:

$$i_d(x, y) = o(x, y) * PSF_d(x, y). \quad (6)$$

the relationship in the frequency domain is:

$$I_d(u, v) = O(u, v) \bullet OTF_d(u, v). \quad (7)$$

$$PSF_d(u, v) = \left| FT^{-1}(P_d(u, v)) \right|^2. \quad (8)$$

$$P_d(u, v) = A(u, v) \exp(i(\phi(u, v) + \phi_d(u, v))). \quad (9)$$

In the above equations, $\phi_d(u, v)$ is the known defocus amount introduced which can be represented by the fourth term representing the defocus amount in the Zernike polynomial, b is a known constant in the experiment:

$$\phi_d(u, v) = b \bullet c_4(u, v). \quad (10)$$

The evaluation function is defined according to the maximum likelihood theory [9] to evaluate the degree of correlation between the reconstructed image and the actual image. The evaluation function's expression is given by Eq. (11).

$$E(o, a) = [i(x, y) - o(x, y) * PSF(x, y)]^2 + [i_d(x, y) - o(x, y) * PSF_d(x, y)]^2. \quad (11)$$

according to Parseval theory and convolution theory

$$E(O, a) = [I(u, v) - O(u, v)OTF(u, v)]^2 + [I_d(u, v) - O(u, v)OTF_d(u, v)]^2. \quad (12)$$

under the following conditions

$$\frac{\delta E(O, a)}{\delta O} = 0, \quad (13)$$

further derivation [5]

$$E(a) = \sum_{u \in X, v \in Y} \frac{|I(u, v)OTF_d(u, v) - I_d(u, v)OTF(u, v)|^2}{|OTF(u, v)|^2 + |OTF_d(u, v)|^2}. \quad (14)$$

If there is noise, then (1) becomes

$$i^*(x, y) = o(x, y) * PSF(x, y) + n(x, y). \quad (15)$$

further derivation

$$i_d^*(x, y) = o(x, y) * PSF_d(x, y) + n_d(x, y). \quad (16)$$

further derivation

$$E(a) = \sum_{u \in X, v \in Y} \frac{|I^*(u, v)OTF_d(u, v) - I_d^*(u, v)OTF(u, v)|^2}{|OTF(u, v)|^2 + |OTF_d(u, v)|^2}. \quad (17)$$

Here, $i(x, y)$ is the intensity distribution of the image with noise on the focal plane, $i_d^*(x, y)$ is the intensity distribution of the image with noise on the defocus plane.

From Eq. (16) and Eq. (17), we can see that the noise data in the in-focus image and the noise data in the defocus image participate in the settlement of the PD algorithm, but the noise is not in accordance with the operation in the PD algorithm, this will greatly reduce the settlement accuracy of the PD algorithm. So the denoising algorithm could be applied to noisy focused and defocused images as a preprocessing stage to improve the robustness of the PD algorithm to noise.

further derivation

$$E(a) = \sum_{u \in X, v \in Y} \frac{|S(u, v)OTF_d(u, v) - S_d(u, v)OTF(u, v)|^2}{|OTF(u, v)|^2 + |OTF_d(u, v)|^2}. \quad (18)$$

Here, we record the in-focus image obtained by the denoising algorithm as $s(x, y)$, defocus image obtained by the denoising algorithm as $s_d(x, y)$, $S(u, v)$ is the Fourier transform of the $s(x, y)$, $S_d(u, v)$ is the Fourier transform of the $s_d(x, y)$.

Image denoising is an indispensable step in many practical applications, the purpose of image denoising is to recover data x from a noise observation y that follows the image degradation model $y = x + v$, according to Bayesian, when the likelihood is known, the priori modeling of the image will play a central role in image denoising. In the past few decades, various models have been used for image prior modeling, sparse models [10–13], Markov random field (MRF) models [14,15], nonlocal self-similarity (NSS) models [16], gradient models [17]. Although they have achieved good denoising effects, such algorithms are

difficult to achieve high performance without sacrificing computational efficiency. The prior model obtained can get rid of the iterative optimization process in the test phase with the introduction of the cascade of shrinkage fields (CSF) and the trainable nonlinear reaction diffusion (TNRD), but they are limited in the overall characteristics of the captured image structure and the scope of level of noise application. In [18], blocking-matching and 3D filtering is introduced in the wavefront sensing field as a preprocessing stage, this method realizes the denoising of unknown noise by directly modeling the priori of image by the noise image. However, the image prior modeling of this algorithm relies on artificial experience, and the complete features of the image are difficult to obtain. This means that although the algorithm has certain effects, there is still much room for improvement. In [19], several metrics that utilize regularizations based on the object and noise power spectra have been introduced into the PD algorithm of low signal-to-noise ratio, but the metrics also rely on artificial experience, so this algorithm has the same problem.

Deep denoising convolutional neural networks (DnCNNs) [20] was first used as an image denoiser, the proposed very deep CNN [21] regard image denoising as a simple discriminative learning problem, implicitly removes the latent clean image with the operations in the hidden layers.

In this study, a denoising strategy based on deep convolutional neural networks with residual learning is first introduced into the PD technique to improve the robustness of PD algorithm to gaussian white noise. This neural network structure evolved from the VGG network. The model training uses residual learning formulas and combines with batch standardization to achieve fast training and improve denoising performance.

This network structure consists of three types of neural network layers:

- (i) Conv + ReLU: This type of neural network layer is used in the data input layer, which is used to generate 64 feature maps using 64 filters of size $3 \times 3 \times c$, and rectified linear units (ReLU, $\max(0; \cdot)$) are then utilized for nonlinearity.
- (ii) Conv + BN + ReLU: This type of neural network is used in the middle layer of the entire neural network, which includes 64 filters of size $3 \times 3 \times 64$, and BN is added between the Conv and the ReLU.
- (iii) Conv: This type of neural network layer is used for the output layer of the entire neural network, and c filters of size $3 \times 3 \times 64$ is used to reconstruct the output.

Here c represents the number of image channels, i.e., $c = 1$ for gray image and $c = 3$ for color image. The structure of the used deep denoising CNN is shown in the Fig. 1.

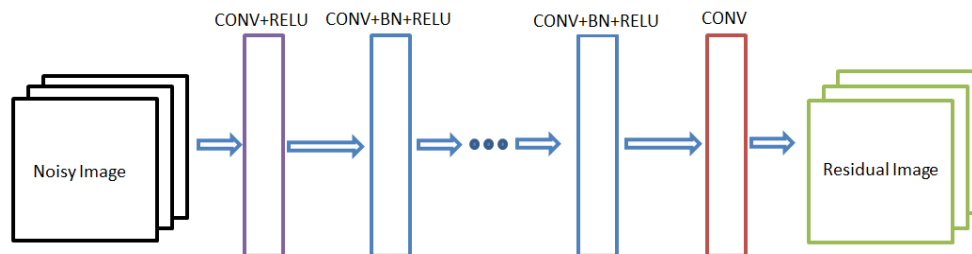


Fig. 1. The structure of the used denoising deep CNN.

For DnCNNs, we train a residual mapping by adopting the residual learning formulation $R(y) \approx v$, and then we have $x = y - R(y)$. Formally, the trainable parameters Θ in DnCNNs can be learned by the loss function which is the averaged mean squared error between the desired residual images and estimated ones from noisy input, here $\{(y_i, x_i)\}_{i=1}^N$ represents N noisy-clean training image (patch) pairs.

$$l(\Theta) = \frac{1}{2N} \sum_{i=1}^N \|R(y_i; \Theta) - (y_i - x_i)\|_F^2. \quad (19)$$

We clip 400 images of size 180×180 in the BDS500 data set to 32×6400 patches of size 64×64 , these images are used as training data set, and the standard deviation of gaussian white noise for the data set is set to $\sigma \in [0 - 0.21]$. We train the three channels of the data set at the same time, so that the well-trained DnCNNs can be applied to RGB image denoising, this ability will increase the settlement range of the PD algorithm [22]. However, in the subsequent simulation experiments, we only used the first channel of the well-trained DnCNNs for the denoising of gray images. An additional hundred images of the BDS500 data set that did not participate in the network training were used as test data set, and some representative test results are given below for clarity.

The number of network layers is 20, and the weights are initialized by the method in [23], and we use SGD with weight decay of 0.0001, the momentum is 0.9, and the small batch size is 32. The learning rate is exponentially decayed from $1e-1$ to $1e-4$.

The CPU we used is Intel(R) Core(TM) i5-4460 K, and the frequency is 3.20 GHz; the graphics processing unit (GPU) we used is NVIDIA GeForce GT 730. The software version of Python is 3.5.2, and the software version of the Tensorflow is tensorflow-gpu-1.4.1, the training time is about 25 hours. The Fig. 2 shows the training results of this neural network recorded using the Tensorboard.

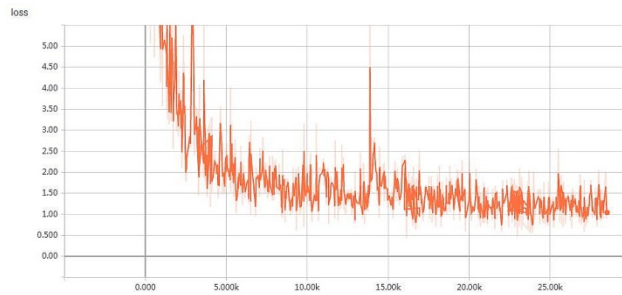


Fig. 2. The training results of deep denoising convolutional neural networks.

3. Numerical simulation

In the simulation experiment, we train DnCNNs with data at different noise levels, and the well-trained DnCNNs has blind denoising ability in the noise training range. Therefore, it is not necessary to perform noise evaluation on the image contaminated by noise before image processing. This ability is not available in many other algorithms.

We randomly introduce four sets of coefficients within certain range. The number of Zernike polynomials is 7 (c4–c10 of the fringe Zernike coefficients), the range of aberration coefficients is $[-0.25\lambda, 0.25\lambda]$. For the set of aberration coefficients, we can use them to generate the in-focus and defocus PSF images with Fourier optics. Gaussian noise is added to the in-focus and defocus images to simulate the real noise conditions. We settle the PD algorithm through improved variable step size adaptive cuckoo search optimization algorithm with $p = 30$, $P_a = 0.25$, the number of nest is 40, the maximum number of iterations is 1000 [9]. The experimental parameters of the numerical simulation are set as follows, the aperture diameter of the optical system is 8 mm, the focal length of the lens is 180 mm, the defocus distance is 1.5 mm, the wave length is 632 nm, and the pixel size of the detector is 5500 nm, $\phi_a(x, y) = \lambda$.

The root mean square error (RMSE) between calculated Zernike coefficients and true Zernike coefficients is calculated as Eq. (20). Where n is the number of the aberration

coefficients considered, and c_i^t are the i -th true aberration coefficients, and c_i^r are the n -th calculated aberration coefficients.

$$RMSE = \left\{ \frac{\sum_{i=4}^{n+4-1} (c_i^t - c_i^r)^2}{n} \right\}^{1/2}. \quad (20)$$

The noise level is indicated by peak signal-to-noise ratio (PSNR) of the degraded defocus and in-focus image.

$$PSNR = \left\{ \frac{MAX(i(x,y)^2)}{\sum_{x=1}^M \sum_{y=1}^N [i(x,y) - i^*(x,y)]^2 / M * N} \right\}^{1/2}. \quad (21)$$

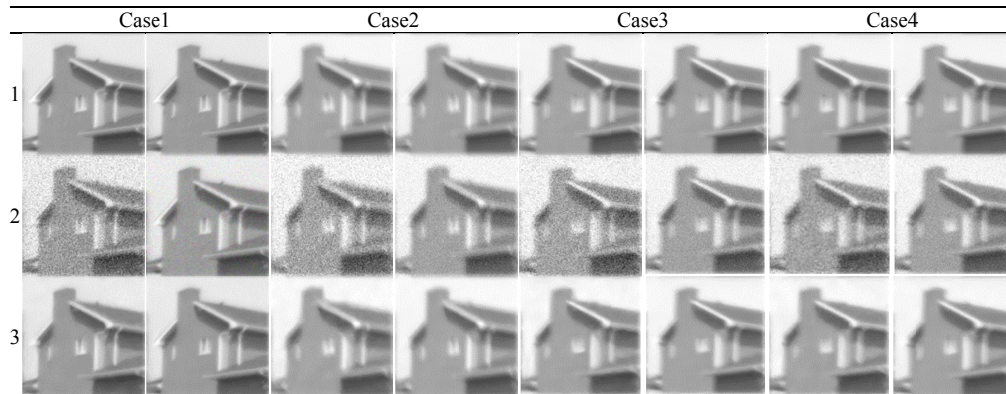
Where $N * M$ indicates the number of total pixels, after calculation in the simulation experiment of this manuscript, the relationship between PSNR and SNR (signal-to-noise ratio) of the degraded defocus and in-focus images is approximately $SNR(dB) \approx PSNR - 4.85$.

The structural similarity index metrics (SSIM) is used as an objective evaluation of image quality.

$$SSIM(f, \hat{f}) = \frac{(2\mu_f \mu_{\hat{f}} + b_1)(2\sigma_{f, \hat{f}} + b_2)}{(\mu_f^2 + \mu_{\hat{f}}^2 + b_1)(\sigma_f^2 + \sigma_{\hat{f}}^2 + b_2)}. \quad (22)$$

where μ is the average, and σ^2 is the variance, f is the pristine object, \hat{f} refers to the estimated object. The constants b_1 and b_2 are used to stabilize the division with a weak denominator.

Table 1. The first row in the table is the ideal in-focus images of the optical system with four sets of wavefront aberration. The second row is the in-focus image contaminated by noise. The third row is the in-focus image which are the denoised image processed by deep CNN. In the second row, for each set of wavefront aberration, there are two kinds of noise images of peak signal to noise ratio, they are 20dB, 30dB.



As can be seen from the Table 1 and Table 2, the overall decline range of average SSIM for the in-focus images contaminated by noise and the ideal in-focus images is 78.28%, 77.98%, 77.44% and 76.78% for each aberration. By contrast, average SSIM remains stable across different noise levels in the improved PD cases. After denoising by the DnCNNs, the overall decline range of average SSIM for of the denoised in-focus images and the ideal in-focus images is 2.81%, 2.62%, 2.64% and 2.55% for each aberration.

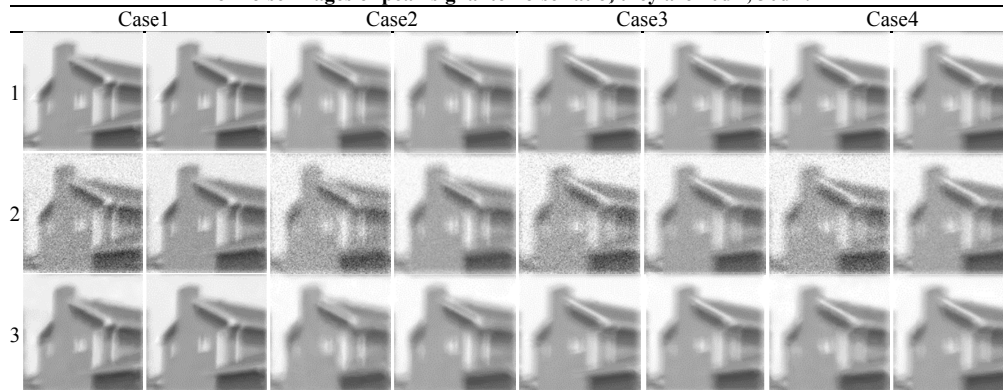
Table 2. The average SSIM values between the in-focus images contaminated by noise and the ideal in-focus images and the average SSIM values between the in-focus denoised images and the ideal in-focus images, within the PSNR range of 40-20 dB for four sets of aberration coefficients.

PSNR	Case1		Case2		Case3		Case4	
	before	after	before	after	before	after	before	after
20	0.2172	0.9719	0.2202	0.9738	0.2256	0.9736	0.2322	0.9745
22	0.2866	0.9776	0.2935	0.9792	0.2953	0.9799	0.2966	0.9791
24	0.3646	0.9821	0.3788	0.9838	0.3776	0.9843	0.3764	0.9837
26	0.4595	0.9857	0.4711	0.9874	0.4671	0.9860	0.4706	0.9864
28	0.5545	0.9888	0.5665	0.9894	0.5650	0.9889	0.5630	0.9888
30	0.6459	0.9903	0.6574	0.9909	0.6548	0.9907	0.6525	0.9908
32	0.7350	0.9918	0.7395	0.9921	0.7356	0.9919	0.7371	0.9919
34	0.8061	0.9928	0.8119	0.9930	0.8098	0.9928	0.8092	0.9930
36	0.8679	0.9931	0.8680	0.9931	0.8659	0.9929	0.8671	0.9930
38	0.9109	0.9931	0.9093	0.9925	0.9101	0.9925	0.9088	0.9926
40	0.9398	0.9939	0.9394	0.9933	0.9398	0.9934	0.9398	0.9934

As can be seen from the Table 3 and Table 4, the overall decline range of average SSIM for the defocus images contaminated by noise and the ideal defocus images is 79.54%, 80.18%, 9.58% and 79.03% for each aberration. By contrast, average SSIM remains stable across different noise levels in the improved PD cases. After denoising by the DnCNNs., the overall decline range of average SSIM for the denoised defocus images and the ideal defocus images is 2.78%, 2.62%, 2.72% and 2.56% for each aberration.

Therefore, the image noise of the in-focus image and the defocus image are effectively removed, making accurate settlement of the subsequent PD algorithm possible.

Table 3. The first row in the table is the ideal defocus images of the optical system with four sets of wavefront aberration. The second row is the defocus images contaminated by noise. The third row is the defocus images which are the denoised image processed by deep CNN. In the second row, for each set of wavefront aberration, there are two kinds of noise images of peak signal to noise ratio, they are 20dB, 30dB.



As can be seen from the Fig. 3, the mean RMSE of the phase estimation for the improved PD algorithm are reduced by 78.48%, 82.35%, 71.09% and 73.67% compared with the mean RMSE for the phase estimation of the traditional PD algorithm across noise levels ranging from 40 dB to 20 dB for four sets of aberration coefficients.

Therefore, simulation experiments show that compared with the traditional PD algorithm, the improved PD algorithm has better performance under various noise levels.

Table 4. The average SSIM values between the defocus images contaminated by noise and the ideal defocus images and the average SSIM values between the defocus denoised images and the ideal defocus images, within the PSNR range of 40-20 dB for four sets of aberration coefficients.

PSNR	Case1		Case2		Case3		Case4	
	before	after	before	after	before	after	before	after
20	0.2048	0.9722	0.1982	0.9738	0.2042	0.9728	0.2097	0.9744
22	0.2741	0.9792	0.2692	0.9785	0.2791	0.9788	0.2761	0.9786
24	0.3577	0.9832	0.3590	0.9836	0.3638	0.9836	0.3670	0.9828
26	0.4515	0.9864	0.4539	0.9868	0.4585	0.9866	0.4629	0.9861
28	0.5454	0.9888	0.5574	0.9892	0.5633	0.9891	0.5639	0.9886
30	0.6434	0.9907	0.6555	0.9908	0.6559	0.9904	0.6580	0.9906
32	0.7326	0.9921	0.7392	0.9916	0.7466	0.9918	0.7408	0.9919
34	0.8054	0.9929	0.8140	0.9924	0.8158	0.9923	0.8159	0.9922
36	0.8651	0.9934	0.8698	0.9927	0.8701	0.9921	0.8699	0.9925
38	0.9085	0.9930	0.9097	0.9926	0.9112	0.9925	0.9111	0.9923
40	0.9401	0.9939	0.9391	0.9934	0.9394	0.9935	0.9395	0.9933

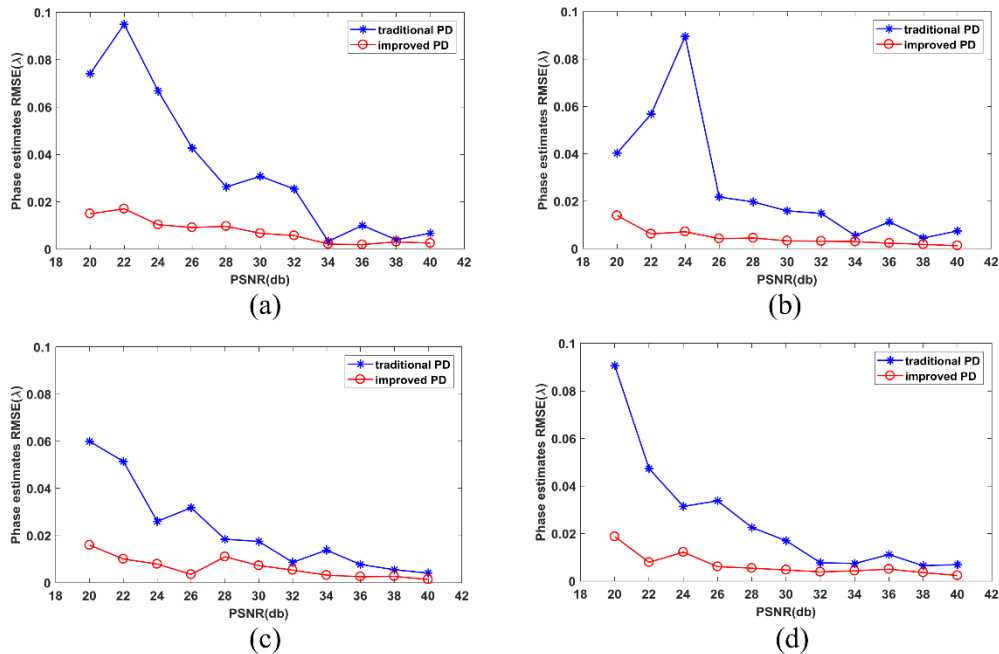


Fig. 3. The RMSEs between the true Zernike coefficients and calculated Zernike coefficients under different PSNR for four sets of aberration coefficients.

4. Conclusion

Image noise will have a great impact on the accuracy of PD algorithm. To improve the robustness of traditional PD algorithm to noise, we use the deep denoising convolutional neural network to preprocess the noise-contaminated in-focus image and defocus in the PD algorithm. The simulation results show that the improved PD algorithm which is added to the DnCNN has better performance than the traditional PD algorithm in RMSE of phase estimation and SSIM across noise levels ranging from 40 dB to 20 dB for several sets of aberration coefficients. In the future, we will carry out related experiments for further verification.

Funding

National Natural Science Foundation of China (NSFC) (11703027).

References

1. J. A. Koch, R. W. Presta, R. A. Sacks, R. A. Zacharias, E. S. Bliss, M. J. Dailey, M. Feldman, A. A. Grey, F. R. Holdener, J. T. Salmon, L. G. Seppala, J. S. Toeppen, L. Van Atta, B. M. Van Wouterghem, W. T. Whistler, S. E. Winters, and B. W. Woods, "Experimental comparison of a Shack-Hartmann sensor and a phase-shifting interferometer for large-optics metrology applications," *Appl. Opt.* **39**(25), 4540–4546 (2000).
2. M. J. Booth, "Adaptive optical microscopy: the ongoing quest for a perfect image," *Light: Sci. Appl.* **3**(4), e165 (2014).
3. R. A. Gonsalves, "Phase Retrieval And Diversity In Adaptive Optics," *Opt. Eng.* **21**, 215829 (1982).
4. P. M. Johnson, M. E. Goda, and V. L. Gamiz, "Multiframe phase-diversity algorithm for active imaging," *J. Opt. Soc. Am. A* **24**(7), 1894–1900 (2007).
5. R. Paxman, B. Thelen, and J. H. Seldin, "Phase-diversity correction of turbulence-induced space-variant blur," *Opt. Lett.* **19**, 1231–1233 (1994).
6. D. J. Lee, B. M. Welsh, M. C. Roggemann, and B. L. Ellerbroek, "Diagnosing unknown aberrations in an adaptive optics system by use of phase diversity," *Opt. Lett.* **22**(13), 952–954 (1997).
7. H. Akaike, "Information Theory and an Extension of the Maximum Likelihood Principle," in *Selected Papers of Hirotugu Akaike*, E. Parzen, K. Tanabe, and G. Kitagawa, eds. (Springer New York, 1998), pp. 199–213.
8. A. C. Sobieranski, F. Inci, H. C. Tekin, M. Yuksekkaya, E. Comunello, D. Cobra, A. von Wangenheim, and U. Demirci, "Portable lensless wide-field microscopy imaging platform based on digital inline holography and multi-frame pixel super-resolution," *Light Sci. Appl.* **4**(10), e346 (2015).
9. D. Li, S. Xu, X. Qi, D. Wang, and X. Cao, "Variable step size adaptive cuckoo search optimization algorithm for phase diversity," *Appl. Opt.* **57**(28), 8212–8219 (2018).
10. M. Elad, and M. Aharon, "Image Denoising Via Sparse and Redundant Representations Over Learned Dictionaries," *IEEE Trans. Image Process.* **15**, 3736–3745 (2007).
11. G. Eraslan, L. M. Simon, M. Mircea, N. S. Mueller, and F. J. Theis, "Single-cell RNA-seq denoising using a deep count autoencoder," *Nat. Commun.* **10**(1), 390 (2019).
12. L. Nasser and T. Boudier, "A novel generic dictionary-based denoising method for improving noisy and densely packed nuclei segmentation in 3D time-lapse fluorescence microscopy images," *Sci. Rep.* **9**(1), 5654 (2019).
13. D. Wu, C. Yang, P. Zhang, Z. Xu, H. Xu, X. Zhang, Z. Cao, Q. Mu, and L. Xuan, "Phase diversity technique with sparse regularization in liquid crystal adaptive optics system," *J. Astro. Tele., Instr., Syst.* **4**, 1–8 (2018).
14. S. Huang, W. Huang, and T. Zhang, "A New SAR Image Segmentation Algorithm for the Detection of Target and Shadow Regions," *Sci. Rep.* **6**(1), 38596 (2016).
15. S. Li, *Markov Random Field Modeling in Image Analysis* (Springer, 2001).
16. K. Dabov, A. Foi, V. Katkovnik, and K. Egiazarian, "Image Denoising by Sparse 3-D Transform-Domain Collaborative Filtering," *IEEE Trans. Image Process.* **16**(8), 2080–2095 (2007).
17. Y. Weiss and W. T. Freeman, "What makes a good model of natural images?" in *2007 IEEE Conference on Computer Vision and Pattern Recognition* (2007), pp. 1–8.
18. H. Yu, C. Yang, X. Zihao, P.-G. Zhang, H. Xu, Z. Cao, Q. Mu, and I. Xuan, "Analysis and reduction of errors caused by Poisson noise for phase diversity technique," *Opt. Express* **24**, 22034–22042 (2016).
19. M. R. Bolcar and J. R. Fienup, "A Comparison of Regularized Metrics for Phase Diversity," in *Frontiers in Optics 2008/Laser Science XXIV/Plasmonics and Metamaterials/Optical Fabrication and Testing* (Optical Society of America, 2008), p. FMM1.
20. K. Zhang, W. Zuo, Y. Chen, D. Meng, and L. Zhang, "Beyond a Gaussian Denoiser: Residual Learning of Deep CNN for Image Denoising," *IEEE Trans. Image Process.* **26**(7), 3142–3155 (2017).
21. K. Simonyan, and A. Zisserman, "Very Deep Convolutional Networks for Large-Scale Image Recognition," arXiv:1409.1556 (2014).
22. D. Li, S. Xu, D. Wang, and D. Yan, "Large-scale piston error detection technology for segmented optical mirrors via convolutional neural networks," *Opt. Lett.* **44**(5), 1170–1173 (2019).
23. K. He, X. Zhang, S. Ren, and J. Sun, "Delving Deep into Rectifiers: Surpassing Human-Level Performance on ImageNet Classification," in *2015 IEEE International Conference on Computer Vision (ICCV)* (IEEE, 2015), pp. 1026–1034.